Atmos. Meas. Tech. Discuss., 8, 4769–4816, 2015
www.atmos-meas-tech-discuss.net/8/4769/2015/
doi:10.5194/amtd-8-4769-2015

Atmospheric Measurement Techniques Discussions

Determining air pollutant emission rates based on mass balance using airborne measurement data over the Alberta oil sands operations

M. Gordon[1,*], S.-M. Li[1], R. Staebler[1], A. Darlington[1], K. Hayden[1], J. O'Brien[1], and M. Wolde[2]

[1]Air Quality Process Research Section, Air Quality Research Division, Environment Canada, Toronto, Canada
[2]National Research Council, Ottawa, Canada
[*]now at: Earth and Space Science and Engineering, York University, Toronto, Canada

Received: 19 February 2015 – Accepted: 20 April 2015 – Published: 11 May 2015

Correspondence to: M. Gordon (mgordon@yorku.ca) and S.-M. Li (shao-meng.li@ec.gc.ca)

Published by Copernicus Publications on behalf of the European Geosciences Union.

Abstract

Top-down approaches to measure total integrated emissions provide verification of bottom-up, temporally-resolved, inventory-based estimations. Aircraft-based measurements of air pollutants from sources in the Canadian oil sands were made in support of the Joint Canada–Alberta Implementation Plan on Oil Sands Monitoring during a summer intensive field campaign between 13 August and 7 September 2013. The measurements contribute to knowledge needed in support of the Joint Canada–Alberta Implementation Plan on Oil Sands Monitoring. This paper describes a Top-down Emission Rate Retrieval Algorithm (TERRA) to determine facility emissions of pollutants, using SO_2 and CH_4 as examples, based on the aircraft measurements. In this algorithm, the flight path around a facility at multiple heights is mapped to a two-dimensional vertical screen surrounding the facility. The total transport of SO_2 and CH_4 through this screen is calculated using aircraft wind measurements, and facility emissions are then calculated based on the divergence theorem with estimations of box-top losses, horizontal and vertical turbulent fluxes, surface deposition, and apparent losses due to air densification and chemical reaction. Example calculations for two separate flights are presented. During an upset condition of SO_2 emissions on one day, these calculations are within 5 % of the industry-reported, bottom-up measurements. During a return to normal operating conditions, the SO_2 emissions are within 11 % of industry-reported, bottom-up measurements. CH_4 emissions calculated with the algorithm are relatively constant within the range of uncertainties. Uncertainty of the emission rates is estimated as 20 %, which is primarily due to the unknown SO_2 and CH_4 mixing ratios near the surface below the lowest flight level.

1 Introduction

Aircraft-based measurements have been previously used to derive emission rates from point and area sources of compounds including CO_2, CH_4, CO, NO_x, and SO_2 (see Ta-

AMTD
8, 4769–4816, 2015

ble 1 for references). This analysis is accomplished by flying downwind and/or around the source, in some cases at multiple heights, and inferring the emissions rate based on a mass-balance analysis. This top-down approach offers an advantage over a bottom-up, inventory-based estimation as it attempts to capture the total integrated emissions, some of which may be missed by inventories or difficult to assess, particularly for large and complex industrial facilities spanning tens to hundreds of square kilometers that are comprised of a large number of activities. Simplifying assumptions may be used in the analysis to reduce the inhibitive cost of aircraft flight time; however, these assumptions result in reduced accuracy of the derived emissions estimates. Flight patterns can be grouped into (a) single-height transects, (b) upwind and downwind spirals, (c) single-screen flights, and (d) box flights. In the latter case, the box can refer to a cylinder, a rectangular cuboid, or any other prism shape that is uniform with height.

The simplest flight pattern, which we refer to as a single-height transect, is a single flight path at one height perpendicular to the mean wind direction and downwind of the point or area sources (Turnbull et al., 2009; Peischl et al., 2013; Karion et al., 2013). This approach assumes a well-mixed boundary layer, such that the species mixing ratio is constant and equal to the measured value between the surface and the boundary layer height. Upwind of the source, the species mixing ratio is assumed to be equal to a constant background value determined either from the outside edges of the downwind transect (Turnbull et al., 2009), or from a second, upwind transect (Peischl et al., 2013; Karion et al., 2013). Uncertainties in the calculated emission rate based on this approach are estimated as ±50 % (Peischl et al., 2013; Karion et al., 2013).

The vertical variation in mixing ratio can be determined by flying in an ascending or descending spiral pattern upwind and downwind of a source (Wratt et al., 2001). This gives the total emission rate of a surface line source connecting the two spiral locations. This approach is ideal for large area sources with little variation in emission rate perpendicular to the wind direction. Uncertainties in the calculated emission rate based on this approach are estimated as ±40 % (Wratt et al., 2001).

AMTD
8, 4769–4816, 2015

For the single-screen method, horizontal and vertical variation in mixing ratio can be accounted for by flying perpendicular to the mean wind direction and downwind of an area source at multiple heights (Cambaliza et al., 2013; Mays et al., 2009). Each traverse follows the same path above the surface at a different height, which allows the measurements to be interpolated to a two-dimensional screen normal to the mean horizontal wind direction. The upwind, background mixing ratio is estimated from the lateral edges of the screen, which are assumed to be located far enough from the area source to contain no emissions from that source. Uncertainties for this method are conservatively estimated at ±50 % (Cambaliza et al., 2013). Cambaliza et al. (2013) reanalyzed their results using the single-height transect method and estimated the uncertainty based on that approach as ranging from 23 to 65 %. The single screen method can also be approximated by flying at a single height above the boundary-layer and measuring a species profile to the surface using a remote sensing such as a Differential Optical Absorption Spectroscopy (DOAS) instrument (Walter et al., 2012). It is unclear what the uncertainty is based on this approach.

The box method expands on the screen method by including multiple screens upwind and surrounding the emissions area (Kalthoff et al., 2002; Alfieri et al., 2010). This analysis is accomplished by flying a square (Alfieri et al., 2010) or a polygon (Kalthoff et al., 2002) pattern around the emissions area and repeating the pattern at multiple heights. The box method refers to either cuboid or other prism shapes, although a cylindrical spiral would follow a similar methodology. Species mixing ratios are interpolated between the multiple flight-path heights and extrapolated to the ground to give a two-dimensional screen or wall surrounding the emissions area (the lateral sides of the box). A mass balance approach is then employed to derive the emission rate within the enclosed volume by calculating the total advective fluxes of the emitted material though the surrounding screen. A model comparison (Panitz et al., 2002) of the Kathoff et al. (2002) study concluded that the advective fluxes account for between 85 and 95 % of the total emissions, suggesting a much lower uncertainty compared to the single height transect or single screen methods described above.

AMTD
8, 4769–4816, 2015

In this paper, we present an algorithm for calculating the emissions from an area source using the box method. We attempt to improve upon the analysis of Kalthoff et al. (2002) and Alfieri et al. (2010) by investigating all possible sources of error and through modified extrapolation of the measurements to the near surface, below the lowest flight path. We have named this improved algorithm the Top-down Emission Rate Retrieval Algorithm (TERRA). Aircraft-based measurements of air pollutants were made during a summer intensive field campaign between 13 August and 7 September 2013 and support the Joint Canada–Alberta Implementation Plan on Oil Sands Monitoring. We use SO_2 and CH_4 to test TERRA from two flights around a facility in the oil sands region on two separate days. Using TERRA with the appropriately designed flight paths allows us to demonstrate improvements on the uncertainties in emission estimates compared to the previously reported aircraft top-down emission estimate methods. SO_2 and CH_4 are chosen as example in these analyses as they represent respectively emissions from a stack source with a low background level and emissions from ground area source with a relatively high background level. Uncertainties due to the method of interpolation and extrapolation are estimated using one of the flight paths with simulated plumes. Sensitivity of the estimation to uncertainties in mixing ratio, wind speed, and various algorithm parameters is analyzed, and SO_2 emission rates are compared to industry reported, bottom-up measurements.

2 Methods

2.1 Aircraft and instrumentation

Instrumentation was installed aboard the National Research Council of Canada Flight Research Laboratory (NRC-FRL) Convair-580 research aircraft. The Convair-580 is equipped to measure horizontal wind speeds (U) and direction with an AIMMS-20 probe (Aventech Inc.). Temperature (T) and vertical wind speeds (w) are measured with a Rosemount 858 probe. Latitude (y) and longitude (x) are measured with a Hon-

AMTD
8, 4769–4816, 2015

eywell IMU. Dewpoint temperature (T_d) is measured with an Edgetech Hygrometer, and altitude (calculated as ellipsoid height altitude, z) and pressure (P) are measured with a DigiQuartz sensor. Additional instrumentation installed specifically for this study comprised a comprehensive suite of fast response instruments to measure gases and aerosols. This paper uses measurements of SO_2 and CH_4 to demonstrate the mass balance approach to estimate emission rates.

SO_2 measurements were made with a Thermo Scientific 43*i*TLE analyzer. The SO_2 instrument was calibrated three times throughout the project, demonstrating a precision of 0.9 % (SD of the three calibration slope measurements). CH_4 measurements were made with a Picarro G2204 cavity-ring-down spectrometer (Picarro, Inc.). The CH_4 instrument was calibrated five times throughout the project, demonstrating a precision of 1.3 % (SD of the five calibration slope measurements). The time delay of the instruments (relative to the wind speed and aircraft state parameter measurements) was measured using automated switching in laboratory experiments with the same inlet systems that were used on the aircraft (including all inlet plumbing configurations). The total delay including instrument response time was 6 s for the SO_2 instrument and 8 s for the CH_4 instrument.

2.2 Study area

The aircraft flew a total of 22 flights over the Athabasca oil sands region in northern Alberta between 13 August and 7 September 2013. Thirteen flights included area emissions investigations, comprising a total of 21 box flights around 7 separate oil sands facilities, mostly surface mining operations. Each box flight path was designed to include one facility only and box flights were only done during directionally consistent winds with speeds $> 5\,m\,s^{-1}$. For this paper, data from two flights surrounding the Canadian Natural Resources Limited (CNRL) Horizon oil sands mining and upgrading facility are analyzed in order to construct an algorithm for the box method and to estimate the uncertainties in the resulting emission rates.

AMTD
8, 4769–4816, 2015

The CNRL Horizon processing facility is located near 57.34° N, 111.75° W, approximately 4 km west of the Athabasca River and 70 km NNW of Fort McMurray, Alberta, Canada. It is a relatively isolated facility, with only boreal forest to the west and north for hundreds of km. Production at the CNRL Horizon facility in 2013 was approximately 100 000 oil barrels day^{-1} (5.8×10^{9} L yr^{-1}, www.cnrl.com, 2014). In 2012, the Horizon facility emitted an average of 6.7 t d^{-1} (metric tonnes per day) of SO_2 (Canadian Natural Resources Ltd, 2014). The flight dates of 20 August and 2 September were chosen as comparative tests of the emissions algorithm because the SO_2 scrubbing unit was temporarily offline on 20 August. During this event, CNRL reported an average of 12.9 t h^{-1} of SO_2 released for the 6 h period from 12:00 to 18:00 LT (MDT) on 20 August, which is compared to a CNRL reported release of 0.17 t h^{-1} of SO_2 for the 6 h period from 12:00 to 18:00 LT on 2 September, during normal SO_2 scrubber operation.

2.3 Mass conservation equations

Emissions are determined by flying in a pattern that approximates a rectangular box shape surrounding the facility area. Some other flights during the airborne study used five-sided polygon shapes. The number and orientation of the box walls has no effect on the analysis discussed herein. For simplicity, the walls of the box for the 20 August and 2 September flights were aligned with the north, south, east, and west directions, regardless of wind direction. Figure 1 illustrates the path of the 20 August and 2 September flights from Fort McMurray to the facility and the box surrounding the facility. The box walls are approximately 5 to 10 km from the edges of the facility boundaries. The 20 August flight also included two profiles from spirals in the north–east (downwind) and south-west (upwind) corners of the box as well as three north–south transects over the facility. The 2 September flight includes a spiral profile at the south wall (downwind) of the box, a second profile near the east wall (upwind) of the box, and two north–south transects over the facility.

AMTD
8, 4769–4816, 2015

The following sections describe the Top-down Emissions Rate Retrieval Algorithm (TERRA) developed herein and used to calculate emission rates from these flight data. Area emission rates are estimated using the Divergence Theorem, which equates the change in mass within a control volume with the integrated mass flux through the walls of the control volume. This gives a mass balance in the control volume for a given compound (C) of

$$E_C = E_{C,\mathrm{H}} + E_{C,\mathrm{HT}} + E_{C,\mathrm{V}} + E_{C,\mathrm{VT}} + E_{C,\mathrm{VD}} - E_{C,\mathrm{M}} - E_{C,\mathrm{X}}, \quad (1)$$

where E_C is the total emissions rate integrated over all activities within the facility, $E_{C,\mathrm{H}}$ is the horizontal advective flux through the box walls, $E_{C,\mathrm{HT}}$ is the horizontal turbulent flux through the box walls, $E_{C,\mathrm{V}}$ is the vertical advective flux through the box top, $E_{C,\mathrm{VT}}$ is the turbulent flux through the box top, $E_{C,\mathrm{VD}}$ is the deposition to the surface, $E_{C,\mathrm{M}}$ is the increase in mass within the volume due to a change in air density, and $E_{C,\mathrm{X}}$ is the increase in mass due to chemical changes of the compound within the box volume. For comparative purposes $E_{C,\mathrm{H}}$ can be separated into inwards and outwards fluxes such that $E_{C,\mathrm{H}} = E_{C,\mathrm{H,out}} - E_{C,\mathrm{H,in}}$, where subscript out denotes horizontal advective flux leaving the box and in denotes horizontal advective flux entering the box. Similarly, the mass balance for air in the control volume is

$$0 = E_{\mathrm{air,H}} + E_{\mathrm{air,V}} - E_{\mathrm{air,M}}, \quad (2)$$

where $E_{\mathrm{air,H}}$ is the horizontal advective flux of air, $E_{\mathrm{air,V}}$ is the box-top advective flux of air, and $E_{\mathrm{air,M}}$ is the change in air mass within the volume. The horizontal advective flux can also be separated as $E_{\mathrm{air,H}} = E_{\mathrm{air,H,out}} - E_{\mathrm{air,H,in}}$.

2.4 Position mapping and interpolation

Figure 2 demonstrates the process by which the 1 s flight position data for the 20 August flight are mapped to the 2-dimensional screen, which comprises the lateral box walls. First the box flight position data are separated from the other flight sections (e.g. to and

AMTD
8, 4769–4816, 2015

from the airport, spirals, transects) by visual inspection. The flight time for the 20 August box was 2 h and 10 min and the flight time for the 2 September box was 1 h and 48 min. In each case, a single horizontal path with four linear components (corresponding to the east, north, west, and south walls) is determined using a least-squares fitting as a function of latitude and longitude (Fig. 2b). The corners of the box path are rounded with a turning radius to produce a smooth path without discontinuities, which further allows a proper calculation of wind speed normal to the curved path at the corners (see Sect. 2.5). The start of the horizontal path is arbitrarily defined as the south-east corner and the horizontal path distance (s) increases in a counter clockwise direction. The selection of the starting position for the horizontal path has no effect on the overall calculation. Each 1 s aircraft position datum during the box flight is then mapped to the closest position on the least-squares path fit. This procedure results in a translation of each flight position point from a 3-dimensional position of latitude (y), longitude (x), and altitude (z, above mean sea-level) to a 2-dimensional screen position of horizontal path distance $s = f(x,y)$, and altitude, z, as shown in Fig. 2c. Herein the term screen is used to refer to the full unwrapped composite of the four walls (with dimensions $s \times z$), whereas wall refers to each of the four box sides.

The wind speeds are separated into northerly and easterly components ($U_N(s,z)$, $U_E(s,z)$). The air density ($\rho_{air}(s,z)$) is calculated at each aircraft position as (Rogers and Yau, 1996)

$$\rho_{air} = \frac{p}{RT(1+0.6\chi_{H_2O})}, \text{ with } \chi_{H_2O} = \frac{A_d \varepsilon}{p} \exp\left(\frac{T_d}{B_d}\right), \quad (3)$$

where $R = 287.1\,\mathrm{J\,kg^{-1}\,K^{-1}}$, χ_{H_2O} is the water vapour mixing ratio, $A_d = 3.41 \times 10^9$ kPa, $B_d = 5420$ K, $\varepsilon = 0.622$, and T, p, and T_d are the measured temperature, pressure, and dew-point temperature, respectively. Five interpolated s-z screens are created for each flight: U_N, U_E, ρ_{air}, SO_2 mixing ratio (χ_{SO_2}), and CH_4 mixing ratio (χ_{CH_4}).

Interpolation of the screens can be done with a variety of methods. Three techniques are compared using simulate plumes in Sect. 3.2: inverse distance weight-

AMTD
8, 4769–4816, 2015

ing (IDW), natural neighbour (Sibson, 1981), and kriging (Isaaks and Srivastava, 1989). Each technique calculates the interpolated values ($\chi(s,z)$) as a weighted average of surrounding points (χ_i) giving $\chi(s,z) = \Sigma(\lambda_i \chi_i)$, with weights $\Sigma\lambda_i = 1$. For IDW, each point in the interpolated image is weighted as the inverse distance to a given power. Initial trials determined that a fourth power gives the best results, which gives $\chi(s,z) = \Sigma d_i^4 \Sigma(\chi_i d_i^{-4})$, where d_i is the distance between the interpolation location and each surrounding data point.

Natural neighbour interpolation creates a Voronoi diagram from the discrete data points. Each point in the interpolated image is used to create an overlapping Voronoi pattern with the surrounding measured data points. The value of the interpolated point is then calculated as a weighted sum average of the surrounding points with weighting equal to the amount of overlap between Voronoi patterns. For this analysis we use the Voronoi image interpolation function from Igor Pro data analysis software (Wavemetrics Inc.).

Kriging requires an approximation of the semivariance, $\gamma(d)$ (half the calculated variance), which is a measure of the variation in measured data points as a function of distance (d) between the points. Here we use what is termed "simple kriging". Each weight is calculated as $\lambda_i = \mathbf{K}^{-1}\mathbf{k}$, where $\mathbf{K}$ is a 2-dimensional matrix with values $\gamma(\infty) - \gamma(d_{i,j})$, and $\mathbf{k}$ is a 1-dimensional matrix with values $\gamma(\infty) - \gamma(d_i)$. Here $d_{i,j}$ is the distance between measured points i and j, and d_i is the distance between the measured point i and the interpolation location.

Interpolation is done to a resolution of $\Delta s = 40$ m and $\Delta z = 20$ m. All extrapolation between the lowest flight path and the surface is removed as the lack of known boundary conditions near the surface leads to erroneous results, including potentially negative mixing ratios. These removed data (typically a vertical gap of approximately 150 m) are filled using a method dependent on the measured variable. The methods used to fill this gap are discussed in Sect. 3.1.

AMTD
8, 4769–4816, 2015

2.5 Emissions algorithm

The terms of Eqs. (1) and (2) are listed in Table 2 in order of necessary operation to calculate the total emission rate, E_C (where C represents SO_2 or CH_4). The terms are expanded to their integral solutions. M_R is the ratio of the compound molar mass to the molar mass of air, which is 64.07/28.97 for SO_2 and 16.04/28.97 for CH_4. Other variables specific to individual terms are discussed below.

The first term ($E_{air,H}$) is the integrated horizontal advective flux of air mass through the screen. This term is evaluated using the interpolated and surface-gap filled screens of $U_N(s,z)$, $U_E(s,z)$, and $\rho_{air}(s,z)$. Since the screen path length, s, is a function of longitude, x, and latitude, y, the normal wind vector ($U_\perp(s,z)$, positive outwards) is calculated through cross-multiplication as

$$U_\perp = \frac{U_N \mathrm{d}s/\mathrm{d}x + U_E \mathrm{d}s/\mathrm{d}y}{\sqrt{(\mathrm{d}s/\mathrm{d}x)^2 + (\mathrm{d}s/\mathrm{d}y)^2}}. \quad (4)$$

The use of a smooth path length with rounded corners (Fig. 2b) allows the lateral flux to be calculated continuously, including the corner locations. The sign of $U_\perp$ is used to separate $E_{air,H}$ into $E_{air,H,in}$ and $E_{air,H,out}$.

The change in air mass within the volume ($E_{air,M}$) is the rate of air mass added to or subtracted from the total box volume due to change in air density with time. The change in air density is dependent on the rate of change of temperature and pressure. This term can be estimated by taking the time derivative of the ideal gas law (see Appendix) and integrating the density term with height to give

$$E_{air,M} = \iiint \frac{d\rho_{air}}{dt} \mathrm{d}x\mathrm{d}y\mathrm{d}z = \frac{A}{\Delta t}\left(\frac{\Delta p}{p} - \frac{\Delta T}{T}\right)\int \rho_{air}\mathrm{d}z, \quad (5)$$

where A is the area enclosed by the box, p and T are the average pressure and temperature, and Δp and ΔT are change in pressure and temperature over the duration of

AMTD
8, 4769–4816, 2015

the box flight (Δt). The average pressure and temperature are approximated as independent of height for this preliminary estimation.

From the estimations of $E_{\mathrm{air,H}}$ and $E_{\mathrm{air,M}}$, the remaining term of Eq. (2) ($E_{\mathrm{air,V}}$), which represents the integrated air mass flux through the top of the box, can be calculated and substituted into $E_{C,\mathrm{V}}$ of Eq. (1). This calculation gives the vertical wind speed at the box-top (w, positive upwards). If it can be demonstrated that the compound mixing ratio at the top of the box ($\chi_{C,\mathrm{Top}}$) is nearly constant, the $E_{\mathrm{air,V}}$ term gives the integrated compound mass flux through the box top.

The $E_{C,\mathrm{H}}$ term in Eq. (1), which represents the integrated lateral mass flux of a compound, can then be solved using the interpolated and surface-gap filled screens of $U_{\mathrm{N}}(s,z)$, $U_{\mathrm{E}}(s,z)$, $\rho_{\mathrm{air}}(s,z)$, and the mixing ratios of $\chi_{\mathrm{SO_2}}(s,z)$ or $\chi_{\mathrm{CH_4}}(s,z)$. As with the air mass flux, the normal wind vector ($U_{\perp}(s,z)$) is calculated from Eq. (4).

The remaining terms ($E_{C,\mathrm{HT}}$, $E_{C,\mathrm{VT}}$, $E_{C,\mathrm{VD}}$, and $E_{C,\mathrm{M}}$) require varying degrees of estimation and their solution is dependent on knowledge of the emissions behaviour and distribution of concentration within the box volume. The results of Panitz et al. (2002) demonstrated the potential relative importance of these terms. Panitz et al. (2002) used a 3-dimensional KAMM/DRAIS model to evaluate the box method for CO and NO_x emissions derived from two flights over a city. The model predicted horizontal turbulent fluxes ($E_{C,\mathrm{HT}}$) no greater than 0.3 % of the total emission rate (E_C) for either CO or NO_x. The vertical turbulent fluxes through the box top ($E_{C,\mathrm{VT}}$) were predicted to be 0.3 % E_C for CO and 0 for NO_x on one flight and 13 % E_C for CO and 6.3 % E_C for NO_x on the other flight, with the high ratios of the second flight likely due to a strong modelled inversion near the box top. Deposition was more consistent with $E_{C,\mathrm{VD}}$ between 2.6 and 3 % E_C for CO and between 5.0 and 6.7 % E_C for NO_x. The change in mass due to temperature and pressure changes was not explicitly stated; however the total change (final box-volume concentration – initial box concentration) was 11.5 and 8.8 % E_C for CO and NO_x on first flight and 3.5 and 3.8 % E_C for CO and NO_x on the second flight.

AMTD
8, 4769–4816, 2015

The horizontal turbulent flux ($E_{C,\mathrm{HT}}$) is proportional to the horizontal diffusion constant (K_x) and the negative change in concentration with downwind distance normal to the screen ($x_\perp$). A Gaussian plume from an elevated source can be assumed to expand approximately linearly with downwind distance (Seinfeld and Pandis, 1998). If it can be assumed that the plume is the only source of horizontal advective flux ($E_{C,\mathrm{H}}$), and the wind direction is perpendicular to the screen wall, the ratio of the horizontal turbulent flux to horizontal advection simplifies to

$$E_{C,\mathrm{HT}}/E_{C,\mathrm{H}} = 2K_x/x_\perp U, \quad (6)$$

where $x_\perp$ is distance downwind of the source, and U is the mean wind speed. For unstable conditions, which is typical for the summer afternoon flight times, the diffusion constant can be estimated as $K_x = 0.1h^{3/4}(-\kappa L)^{-1/3}u_*$, where h is the boundary-layer height, $\kappa = 0.4$, L is the Mono–Obukhov length, and u_* is the friction velocity (Seinfeld and Pandis, 1998).

Vertical turbulent fluxes ($E_{C,\mathrm{VT}}$) will occur at the box-top if there is an inversion near the box-top height. Following Alfieri et al. (2010), the integrated vertical flux due to an inversion step change $\Delta\chi$ can be approximated as $E_{C,\mathrm{VT}} = A\rho_{\mathrm{air}}w_{\mathrm{e}}\Delta\chi$, where A is the box-top area and w_{e} is an entrainment rate, which Alfieri et al. (2010) estimated as 0.01 to 0.03 $\mathrm{m\,s^{-1}}$. The determination of $\Delta\chi$ requires investigation of flight spirals that traverse the boundary-layer height.

The calculation of deposition to the surface ($E_{C,\mathrm{VD}}$) requires an estimation of the deposition velocity (V_{d}) and knowledge of the mixing ratio at the surface (χ_{sur}) throughout the box. The estimation of surface mixing ratio is discussed in Sect. 3.1. As a rough estimate, the deposition rate can be approximated as $E_{C,\mathrm{VD}} = A\rho_{\mathrm{air}}V_{\mathrm{D}}\chi_{\mathrm{Sur}}$, where χ_{Sur} is the average mixing ratio at the surface (i.e. $\chi_{\mathrm{Sur}} = \int\chi(s,z_{\mathrm{g}})\mathrm{d}s/\int\mathrm{d}s$).

The change in species (SO_2 or CH_4) mass within the volume ($E_{C,\mathrm{M}}$) is the rate of species mass added to or subtracted from the total box volume due to change in air density with time. Previous mass-balance approaches (see Table 1 for references) have ignored this and the $E_{a,V}$ term, typically with the justification that meteorological condi-

AMTD
8, 4769–4816, 2015

tions are nearly constant during early afternoon hours when the flights were done. The term cannot be estimated directly from measurement as the distribution of mixing ratio within the box volume is unknown. It can be approximated, following Eq. (4), as

$$E_{C,\mathrm{M}} = M_{\mathrm{R}} \iiint \chi_C \frac{\mathrm{d}\rho_{\mathrm{air}}}{\mathrm{d}t} \mathrm{d}x\mathrm{d}y\mathrm{d}z = \frac{AM_{\mathrm{R}}}{\Delta t}\left(\frac{\Delta p}{p} - \frac{\Delta T}{T}\right) \int \chi_C(z)\rho_{\mathrm{air}}\mathrm{d}z, \quad (7)$$

where $\chi_c(z)$ is approximated as the average screen mixing ratio around the box walls (i.e. $\chi_c(z) = \int \chi_c(s,z)\mathrm{d}s / \int \mathrm{d}s$).

The change in species mass within the volume ($E_{C,\mathrm{X}}$) is the rate of species mass created or lost due to chemical reaction (assuming the emissions are at steady state). If an exponential decay of concentration due to a chemical reaction is assumed, the magnitude of $E_{C,\mathrm{X}}$ can be estimated as $E_{C,\mathrm{X}}/E_{C,\mathrm{H}} = \exp(-t_0/\tau) - 1$ (the negative result indicates a loss of concentration). Here t_0 is the time the species spends within the box and τ is the lifetime of the species.

3 Results

3.1 Near-surface extrapolation

Because the lowest flight path ($z_{\mathrm{L}}(s)$) was typically near 150 m above ground level ($z_{\mathrm{g}}(s)$), and there were no ground level measurements along the flight paths, there is a gap in measurement data between the surface and the lowest flight altitude. For many of the studies listed in Table 1, a well-mixed layer below the lowest flight altitude is assumed. Because surface values are unknown, this can lead to unquantified uncertainties. For both surface based and stack emission sources, without constraints of surface measurements along the box walls, this lack of near-surface measurements may lead to large uncertainties in the emission rate estimations based on the interpolation schemes. To reduce these uncertainties, we estimate variables near the surface

AMTD
8, 4769–4816, 2015

region with an extrapolation scheme based on known boundary layer meteorological empirical approximations.

3.1.1 Wind speeds

From flux–gradient relations, it can be shown that wind speeds follow a stability dependent log profile (Garrett, 1996) which can be compared to a least squares fit of U to $\ln(z)$ as

$$U(z) = \frac{u_*}{\kappa}\left(\ln\left(\frac{z - z_g - d}{z_0}\right) - \Psi\right) = \frac{u_*}{\kappa}\ln\left(z - z_g - d\right) + f\left(u_*, z_0, \Psi\right). \quad (8)$$

Here u_* is the friction velocity, $\kappa = 0.4$, z is the flight altitude, z_g is the ground height beneath the flight path, d is a displacement height and z_0 is the roughness length, which are both characteristic of the terrain and surface characteristics, and Ψ is a stability correction, which depends on atmospheric conditions. The terms of the equation which are independent of height are grouped into a least-squares fit parameter f.

The displacement height, d, and the fit parameter, f (which incorporates friction velocity, roughness length, and stability), is approximated using measurements from a nearby WindRASS (Scintec) acoustic profiler. The profiler was located in Fort Mckay during the project at 57.19° N, 111.64° W, approximately 18 km SSE of the flight tracks. The profiler measures winds from a height above ground of 40 m to as high as 800 m (in ideal conditions) in 15 min averages. During the 20 August and 2 September flight times (09:58 to 13:34 and 11:18 to 14:43 LT, respectively) the maximum profiler measurement height ranged from 220 to 450 m above ground level. For consistency, we limit the data to a height of 220 m, since we are interpolating only the lowest 150 m of the wind screens. The wind measurements during the 20 August and 2 September flight times were averaged and a least squares fit to Eq. (8) was determined. This fitting gives values of $d = 6.0\,\mathrm{m}$, $u_* = 0.60\,\mathrm{m\,s^{-1}}$, and $f = -2.64\,\mathrm{m\,s^{-1}}$ for the 20 August data and $d = 3.1\,\mathrm{m}$, $u_* = 0.68\,\mathrm{m\,s^{-1}}$, and $f = -1.87\,\mathrm{m\,s^{-1}}$ for the 2 September data. Al-

AMTD
8, 4769–4816, 2015

though displacement height, d, should be constant, the difference is small relative to the vertical resolution of the interpolated wind screens ($\Delta z = 20\,\mathrm{m}$). Comparing these averaged fits with the 15 min measurements (over the 40 to 220 m height range) for the same time periods gives root-mean squared errors of 0.78 and $1.16\,\mathrm{m\,s^{-1}}$ for wind speeds for the 20 August and 2 September flight times respectively.

To interpolate the wind speeds between the surface and the lowest flight height, the friction velocity is determined from each interpolated s-z wind screen. At each s location (with resolution $\Delta s = 40\,\mathrm{m}$), Eq. (8) is solved for u_* with wind data from the lowest flight path ($U(z_\mathrm{L})$, where typically $z_\mathrm{L} - z_\mathrm{g} \cong 150\,\mathrm{m}$), and d and f values as determined above. Wind speed data are then filled in at each s location for $z_\mathrm{g} < z < z_\mathrm{L}$ from Eq. (8).

3.1.2 Air density

Although air density varies exponentially with height (amsl), at low altitudes (less than several km), it can be approximated with a linear dependence on altitude ($\rho_\mathrm{air}(z) = a + bz$). The measured air density from the 20 August flight varies linearly with z and correlates as $r^2 = 0.993$ ($a = 1.184\,\mathrm{kg\,m^{-3}}$ and $b = -1.0 \times 10^{-4}\,\mathrm{kg\,m^{-4}}$), and the measured air density from the 20 August flight varies linearly with z with $r^2 = 0.990$ ($a = 1.185\,\mathrm{kg\,m^{-3}}$ and $b = -9.2 \times 10^{-5}\,\mathrm{kg\,m^{-4}}$). The gap of $z_\mathrm{g}(s) < z < z_\mathrm{L}(s)$ is filled for each flight using this linear dependence.

3.1.3 Pollutant mixing ratios

Five methods are compared to extrapolate mixing ratio values to the surface, which are termed: (1) zero, (2) constant, (3) zero-to-constant, (4) linear-fit, and (5) exponential-fit. The zero method assumes an elevated plume that is completely above the lowest measurement height and a zero background concentration, which gives $\chi(s,z) = 0$ for $z_\mathrm{g}(s) < z < z_\mathrm{L}(s)$. The constant method assumes an elevated plume with a constant background level. The background level is derived from the lowest flight measurement

AMTD
8, 4769–4816, 2015

to give $\chi(s,z) = \chi(s,z_L)$ for $z_g(s) < z < z_L(s)$. The zero-to-constant method assumes non-zero concentrations at the lowest flight level, a zero concentration at the surface, and a linear interpolation between the surface and the lowest flight level. This interpolation gives $\chi(s,z) = \chi(s,z_L) \cdot (z - z_g(s))/(z_L(s) - z_g(s))$ for $z_g(s) < z < z_L(s)$.

For a surface based emission or a low plume in which the maximum value is near the surface, the choice of extrapolation method is much more important. For example, emissions of CH_4 from the facility can be from ground sources such as tailings ponds, fugitive emissions from pipe lines, or fresh mine face exposed during continuing mining operations. Hence, the bulk of the emitted CH_4 mass may be below the lowest measurement altitude. The linear-fit method assumes a maximum value mixing ratio at the ground and a linear decrease in mixing ratio with height (z). The rate of change and the surface mixing ratio are determined from a least-squares fit at each s location (with resolution $\Delta s = 40$ m) up to a height (from ground) of $z(s) - z_g(s) = 300$ m. The exponential-fit method also uses the same data range for a least-squares fit, but assumes an exponential decay of

$$\chi(s,z) = \chi_{Top}(s) + (\chi_{sur}(s) - \chi_{Top}(s)) \exp\left((-(z - z_g(s))/z_R(s))^2\right), \quad (9)$$

where $\chi_{sur}(s)$ is the surface mixing ratio and $z_R(s)$ is the scaling distance of the exponential function, both determined by least-squares fitting up to a height (from ground) of $z - z_g(s) = 1000$ m. This method assumes that the surface sourced plume dispersion has a half-Gaussian distribution vertically at locations close to the sources, such as along the box walls.

3.2 Interpolation schemes

To determine the accuracy of the interpolation methods, three simulated emissions scenarios were generated based on: a single elevated source (smoke stack); two nearby sources with overlapping plumes (one tall smoke stack and one smaller stack); and a vertically mixed ground source. All scenarios assume a southerly wind at the location

AMTD
8, 4769–4816, 2015

of this facility. A slant factor (β) is added to the equations to simulate a wind shear with height, resulting in Gaussian distributions of mixing ratio at the north wall of

$$\chi(s,z) = \sum_i \exp\left[-\frac{1}{2}\left(\left(\frac{s - s_{o,i} - \beta z}{\sigma_{s,i}}\right)^2 + \left(\frac{z - z_{o,i}}{\sigma_{z,i}}\right)^2\right)\right]. \quad (10)$$

The values for each scenario are listed in Table 3. The flight path for the 20 August flight is then used to sample the simulated values. Figure 3 shows the mixing ratios for each simulation along the north wall with the flight path locations superimposed. Values on the east, west, and south walls are near zero in all scenarios. Image interpolation (IDW, Nearest Neighbour, and Kriging) is then used with the sampled flight path positions to recreate the original image at a resolution of $\Delta s = 40$ m and $\Delta z = 20$ m. The interpolation analysis is limited to the north wall (12 km $< s <$ 29 km), with values outside this range assumed to be zero.

Interpolated data below the lowest flight path are removed and replaced with near-surface extrapolation as discussed in Sect. 3.1. For the single elevated source, there is clearly no simulated plume in the lowest 150 m (Fig. 3a), and the zero mixing ratio extrapolation method is used. For the two overlapping plumes scenario (Fig. 3b,), there are significant mixing ratio values at the lowest flight level, approaching zero near the surface. Here, the zero, constant, and zero-to-constant mixing ratio extrapolation methods are compared. For the ground source scenario (Fig. 3c), there is an increase in mixing ratio towards the surface, and the linear-fit and exponential-fit methods are chosen for comparison.

A statistical comparison of the three interpolation routines is shown in Table 4. For all scenarios and extrapolation methods, IDW demonstrates the highest r.m.s. error and lowest correlation coefficient, while kriging consistently demonstrates the lowest r.m.s. error and highest correlation coefficient. The best results are obtained for the single elevated plume, with an r.m.s. error of 8.6 % of the average and $r^2 = 0.998$. For the two overlapping plumes with a significant concentration below the lowest flight path, the linear extrapolation to the surface gives the best results, with an r.m.s. error of

AMTD
8, 4769–4816, 2015

13.4 % of the average and r^2 = 0.997. For the ground source scenario, the exponential fit extrapolation gives the best results, with an r.m.s. error of 19.2 % of the average and r^2 = 0.998.

More complex kriging schemes are available that may further improve the accuracy, but these results demonstrate that a far greater source of uncertainty is the extrapolation of the data between the lowest flight level and the surface. In cases where extrapolation is not necessary (e.g. scenario 1), the average interpolated value is within 0.2 % of the simulation average. The other cases require a proper choice of extrapolation technique based on knowledge of the mixing ratio behaviour in this region. For example, the case of an elevated plume with part of the plume beneath the lowest flight is best suited to a zero-to-constant extrapolation of mixing ratio to the surface, while a ground source concentration which decreases with height above the surface is best suited to an exponential-fit extrapolation. Without knowledge of this behaviour, uncertainties due to extrapolation are on the order of $\delta_{Ex} \approx 20\,\%$, based on a comparison of the r.m.s. errors.

3.3 Interpolated mixing ratio screens

Figure 4 shows the mixing ratio screens for SO_2 for the 20 August and 2 September flights. For the 20 August flight (Fig. 4a), the primary source of SO_2 appears to be two separate and elevated smokestack plumes. Due to the elevation of the sources, mixing ratios are generally low at the lowest flight altitudes ($z_L(s)$) and the extrapolated mixing ratios within the gap of $z_g(s) < z < z_L(s)$ are expected to be even lower. For the 2 September flight (Fig. 4b), the apparent plumes are generally lower and extrapolation below the $z_L(s)$ level is required. For an initial base-case we use a zero-to-constant extrapolation of mixing ratio to the surface for both flights, and compare the zero and constant extrapolation techniques in Sect. 4.1. The linear surface extrapolations are shown below the lowest flight paths in Fig. 4a and b.

AMTD
8, 4769–4816, 2015

The interpolated CH_4 screens are shown in Fig. 5. The near-surface behaviour of CH_4 is more complex and more significant than the near surface behaviour of SO_2 as the CH_4 emissions appear to be surface-based. As is shown in Fig. 5, the highest measured values of χ_{CH_4} are near the lowest flight path ($z_L(s)$), clearly indicating surface sources. Hence, the bulk of the emitted CH_4 mass may be below the lowest measurement locations. For a base case analysis we use an exponential fit to extrapolate mixing ratios to the surface and compare other extrapolation methods in Sect. 4.1.

Linear and exponential fits with poor fitting statistics (defined here as $r^2 < 0.1$) for each s location are removed and replaced using the constant extrapolation method. Linear fits which indicate an increase in concentration with height are replaced with constant value extrapolation ($\chi(s,z) = \chi(s,z_L)$ for $z_g(s) < z < z_L(s)$). After the removal of failed fits ($r^2 < 0.1$), the exponential fitting results in average correlation coefficients of $r^2 = 0.79$ for the 20 August flight and $r^2 = 0.92$ for the 2 September flight. The linear fitting of CH_4 (presented in Sect. 4.1) results in an average r^2 value of 0.82 for the 20 August flight and an average r^2 value of 0.84 for the 2 September flight. Examples of the extrapolations for the highest recorded values at $z = z_L(s)$ (for each flight) are shown in Fig. 6. These figures compare the measured values (within ±40 m of the s location), interpolated values, and extrapolations using constant value, linear-fit, and exponential-fit.

3.4 Emission rate calculation

The change in air mass within the volume, $E_{air,M}$, is estimated based on temperature and pressure changes (from Eq. 5) over the duration of the flights as measured at two locations at Fort McMurray Airport (56.650° N, 111.213° W, http://climate.weather.gc.ca) and two meteorological towers (http://www.wbea.org). One tower is 167 m tall (AMS03: 57.032° N, 111.505° W) and the other is 75 m tall (AMS05: 56.969° N, 111.482° W). Both towers are located approximately 40 km from the CNRL facility (nearly half-way between the airport and the facility). The average pressure ratio

AMTD
8, 4769–4816, 2015

from both airport locations is $\Delta p/p = 0.02\,\%$ for 20 August and $\Delta p/p = 0.13\,\%$ for 2 September. The average temperature ratio from the lowest (20 m) and highest (75 or 167 m) tower heights and two airport measurement locations is $\Delta T/T = 0.99\,\%$ for 20 August and $\Delta T/T = -0.69\,\%$ for 2 September. The sensitivity of the final results to the pressure and temperature ratios is discussed in Sect. 4.1. The change in air mass ($E_{\mathrm{air,M}}$) is compared to the horizontal advective flux of air mass ($E_{\mathrm{air,H,in}}$ and $E_{\mathrm{air,H,out}}$) in Table 5. These terms are then used to determine the vertical advective air mass flux ($E_{\mathrm{air,V}}$) from Eq. (2). Dividing the vertical advective air mass flux by the box-top area and an average air density gives an average exit velocity through the box-top of $w = 0.10\,\mathrm{m\,s^{-1}}$ for 20 August and $w = 0.08\,\mathrm{m\,s^{-1}}$ for 2 September. This exit velocity is a result of a divergence of the air flow since flow streamlines over a varying terrain are unlikely to follow flat, horizontal trajectories.

Table 6 lists the integrated lateral flux terms ($E_{C,\mathrm{H,in}}$ and $E_{C,\mathrm{H,out}}$) for SO_2 and CH_4. The value of $E_{\mathrm{air,V}}$ shown in Table 5 is used to calculate the compound mass flow through the box top as $E_{C,\mathrm{V}} = M_{\mathrm{R}}\chi_{C,\mathrm{Top}}E_{\mathrm{air,V}}$. At the highest level of the interpolated screen ($z = 1540\,\mathrm{m}$ for 20 August, $z = 1500\,\mathrm{m}$ for 2 September), the average mixing ratio of SO_2 is near zero for both flights ($< 0.02\,\mathrm{ppb}$). The resulting mass flow of SO_2 through the box-top is negligible compared to the lateral advection through the box walls. The average mixing ratio of CH_4 at the top of the screen is $\chi_{C,\mathrm{Top}} = 1.89\,\mathrm{ppm}$ for the 20 August flight and $\chi_{C,\mathrm{Top}} = 1.91\,\mathrm{ppm}$ for the 2 September flight. This non-zero mixing ratio results in a significant loss of CH_4 through the box top, which is larger than the net gain of CH_4 through the box walls.

The horizontal turbulent flux for a Gaussian plume can be estimated for SO_2 by assuming a linear expansion of the plume width with distance downwind. Based on measured wind profiles, estimated plume height and source location, input variables of Eq. (6) are estimated as $u_* = 0.3\,\mathrm{m\,s^{-1}}$, $h = 1.6\,\mathrm{km}$, $L = 50\,\mathrm{m}$, $x = 4\,\mathrm{km}$, and $U = 6\,\mathrm{m\,s^{-1}}$. These estimates give a ratio of $E_{C,\mathrm{HT}}/E_{C,\mathrm{H}} \sim 0.03\,\%$. For CH_4 the plume location near the ground would suggest a much smaller diffusion constant and wind

AMTD
8, 4769–4816, 2015

speed, resulting in negligible horizontal turbulent flux for these surface based emissions.

For the calculation of the vertical turbulent fluxes ($E_{C,\mathrm{VT}}$), a comparison of flight altitude to SO_2 for the entire flight duration (including vertical spirals to 2 km, as shown in Fig. 1) demonstrates that SO_2, which has background levels near 0, shows no inversion step change ($\Delta\chi$) for either flight. In comparison, during the 20 August flight, there is an inversion step change for CH_4 of approximately 8.0 ppb. The height of this step change varies between 1.0 and 1.8 km a.m.s.l. depending on location. During the 2 September flight, there is a much stronger inversion step change for CH_4 of approximately 28 ppb near 1.5 km a.m.s.l. Using these values with $w_e = 0.03\,\mathrm{m\,s^{-1}}$ gives $E_{C,\mathrm{VT}} = 0.07$ and $0.24\,\mathrm{t\,h^{-1}}$ for 20 August and 2 September, respectively, representing 2 and 6 % of the CH_4 emission rate (E_C) estimated for both days. However, there is a large uncertainty in this $E_{C,\mathrm{VT}}$ estimation and it is unclear from these measurements if the inversion step change occurs near enough to the box top to necessitate inclusion in the calculated emissions.

The deposition term is calculated with a surface mixing ratio (χ_{Sur}) estimated with the same near-surface interpolation schemes used to calculate $E_{C,\mathrm{H}}$. For SO_2, a linear decrease to a zero surface mixing ratio was used, which would give zero deposition. Hence SO_2 deposition is zero for this base case, but will be non-zero for other near surface extrapolation techniques (compared in Sect. 4.1). For example, using the constant value extrapolation with a deposition velocity for SO_2 of $V_D = 10\,\mathrm{mm\,s^{-1}}$ (Zhang et al., 2003) gives depositions of < 2 % of $E_{C,\mathrm{H}}$. For CH_4, generally deposition is not considered in mass balance calculations, although some microbial uptake of CH_4 in soils has been documented (e.g. Whalen and Reeburgh, 2000). Here we assume that the CH_4 deposition rate ($E_{C,\mathrm{VD}}$) is zero.

The change in compound mass within the box volume due to change in air density, $E_{C,\mathrm{M}}$, is estimated from Eq. (7) with the average temperature and pressure ratios used to calculate the $E_{\mathrm{air,M}}$ term using Eq. (5). As discussed in Sect. 2.5, the unknown concentrations within the volume are estimated by averaging the surrounding box at each

AMTD
8, 4769–4816, 2015

height level. The resulting values of $E_{C,M}$ are < 0.2 % of the horizontal flux term $E_{C,H}$ for SO_2 for both days. For CH_4, the resulting values of $E_{C,M}$ are small relative to the horizontal flux term $E_{C,H}$ (±2 % E_C), but are large compared to the final calculated emission rate (−35 and 40 % E_C for 20 August and 2 September respectively). However, it will be demonstrated in Sect. 4.1 that the final emission rate is not strongly dependent on the change in air density due to temperature and pressure changes. This is because the change in density influences both $E_{air,M}$ (Eq. 5) and $E_{C,M}$ (Eq. 7) as is shown in the Appendix.

The change in compound mass within the volume due to oxidation of SO_2 ($E_{C,X}$) is estimated for a source to box-wall distance of 4 km, an average wind speed of U = 6 m s^{-1}, and a chemical lifetime of τ = 24 h (Walter et al., 2012). These estimates give t_0 = 11 min and $E_{C,X}/E_{C,H}$ = −0.8 %. The chemical reaction of CH_4 is assumed to be insignificant.

4 Discussion

4.1 Analysis of uncertainties

Most of the uncertainties in the calculated emission rates are due to four subcomponents: the near-surface extrapolation technique, the temperature and pressure ratios, the near-surface wind extrapolation, and the box-top mixing ratios. For an analysis of the uncertainties caused by these components, the terms listed in Table 2 are recalculated for a number of alternate scenarios for the four components. These recalculated emission rates are compared in Table 7 for SO_2 and Table 8 for CH_4.

For SO_2, the base case was calculated by assuming a linear decrease from the mixing ratio measured at the lowest flight altitude to zero at the surface. Assuming a constant value of $\chi(s,z) = \chi(s,z_L)$ below $z_L(s)$ results in very little change for the 20 August flight, but a substantial increase in emission rate (10 %) for the 2 September flight. Assuming a constant value of $\chi = 0$ below $z_L(s)$ results in very little change for

AMTD
8, 4769–4816, 2015

the 20 August flight, but a substantial decrease (−12 %) for the 2 September flight. As demonstrated by Fig. 4, the plume is well above the lowest flight path on 20 August, but much closer to the surface on 2 September, which increases the uncertainty due to surface extrapolation. A constant value of zero is an extreme assumption, and it is likely that the true profile is somewhere between the constant ($\chi(s,z) = \chi(s,z_L)$) and linear extrapolation techniques.

For CH_4, the base case is an exponential extrapolation below the lowest flight path, which results in surface mixing ratios as high as 1 ppm above background levels on 20 August and 0.5 ppm above background levels on 2 September (typical background levels on both days are near 1.9 ppm). Here, the use of the linear or constant extrapolation techniques (as discussed in Sect. 3.1) has a strong influence on both the 20 August and 2 September results. This dependency on extrapolation method is consistent with the uncertainty of a surface-based emission source and a low altitude plume (as shown in Fig. 5). Large-eddy simulation modeling by Vinuesa and Galmarini (2009) demonstrate that a ground source with a mean wind speed of 5 m s^{-1} develops from an exponential profile to a constant value near the surface within 2 to 6 km distance from the source, suggesting that the constant value extrapolation to the surface may be a better physical representation of the plume. However, under ideal conditions, a constant upwind emission of CH_4 from the upwind boreal forest would result in an exponential vertical profile of mixing ratio going into the box. Hence we propose a fourth method of extrapolation to the surface which uses a combination of the three extrapolation techniques, depending on the flux direction. In situations where air masses pass over the boreal forest and then enters the box, an exponential extrapolation to the surface is used, and when the air mass leaves the box, a constant extrapolation to the surface is used, thereby considering the results of the large eddy simulation modeling (Vinuesa and Galmartini, 2009). This extrapolation method results in a reduction of the emission rate of 27 % from the 20 August base case and a reduction of 15 % from the 2 September base case. Although this method may be a better physical representation, the extrapolation of near surface plumes is a relatively large source of error.

AMTD
8, 4769–4816, 2015

These values are consistent with the uncertainty estimates of $\delta_{Ex} \approx 20\,\%$ determined in Sect. 3.2.

The temperature and pressure ratio difference from Eqs. (5) and (7) ($\Delta p/p - \Delta T/T$) used in the base case is an average of four meteorological stations in the surround area. This term determines the magnitude of the change in air density within the box. The average value is $-0.97\,\%$ on 20 August, indicating a reduction in air density with time, and $0.82\,\%$ on 2 September, indicating an increase in air density with time. Using the minimum and maximum ratios derived from the stations with the highest (or lowest) temperature (or pressure) ratios gives an indication of the uncertainty due to the air density change in the region. The minimum ratios are -1.07 and $-0.45\,\%$, and the maximum ratios are -0.85 and $1.30\,\%$ on 20 August and 2 September, respectively. The derived SO_2 emission rate is not sensitive to variation in air density (due to the low background mixing ratios); however, the CH_4 emission rate does show some dependence, with changes in emission rates between -2 and $5\,\%$ from the base case for the given range of temperature and pressure ratios. Hence, for species with high backgrounds, we estimate an uncertainty of $\delta_{dens} \approx 5\,\%$ due to density changes within the box, while for species with near-zero background $\delta_{dens} \approx 0$.

To estimate sensitivity to the extrapolation of wind speed, the base case scenario was rerun assuming a constant wind speed of $U = U(z_L)$ for $z_g < z < z_L$. The resulting change in the estimated emission rate is approximately $1\,\%$ or less, suggesting that the correct parameterization of wind speed near the surface is not significant. The uncertainty for wind speed is therefore estimated as $\delta_{wind} \approx 1\,\%$.

The assumed constant mixing ratio at the top of the box is estimated using the average measured value at the top of the interpolated screen walls (i.e. $\chi_{C,Top} = \int \chi(s, z_{Top}) ds / \int ds$). This value is then used in the calculation of the vertical advection term, $E_{C,V}$. For a normal distribution of error there is 95 % confidence that the true mean is within approximately $2\sigma/\sqrt{n}$ of the measured mean, where σ is the SD of the measurements and n is the number of samples (measured at a rate of 1 Hz). For both flights there are more than 600 sample points near the box top. For SO_2,

AMTD
8, 4769–4816, 2015

the real mean values of $\chi_{C,\mathrm{Top}}$ are 0 ± 0.026 ppb on 20 August and 0 ± 0.017 ppb on 2 September. For CH_4, the real mean values are 1.89 ppm $\pm$ 0.36 ppb on 20 August and 1.91 ppm $\pm$ 0.82 ppb on 2 September. To estimate the uncertainty in the emission rate due to the assumption of a constant box-top mixing ratio value, the emission rate is recalculated with these ranges of $\chi_{C,\mathrm{Top}}$. The changes in estimated emission rates are shown in Tables 7 and 8. The uncertainty is estimated as $\delta_{\mathrm{Top}} \approx 1\,\%$.

The total uncertainty based on these variations is estimated as

$$\delta^2 = \delta^2_{\mathrm{Ex}} + \delta^2_{\mathrm{dens}} + \delta^2_{\mathrm{wind}} + \delta^2_{\mathrm{Top}}. \quad (11)$$

Using the highest uncertainties gives $\delta \approx 21\,\%$ for CH_4 on both flights and SO_2 on the 2 September flight. This value is dominated by the uncertainty of the extrapolation method. For the case of the clearly elevated SO_2 plume on 20 August, the result is independent of extrapolation method and the background level is near zero. In this case the total uncertainty can be estimated as $\delta \approx 2\,\%$. These results demonstrate that, for any emission type or source location in which the plume is near the lowest flight level, the uncertainty is dominated by the unknown concentration values near the surface.

4.2 Wind consistency

A potential source of error with the SO_2 plume is the assumption of constant wind speed during the box flight. This assumption is less of an issue with CH_4 as it is a surface source and the bulk of the ground-source plume is sampled in the lowest two flight tracks where winds are generally lower. The aircraft took approximately 11 to 12 min to complete one level track around the facility. If there is a shift in mean wind direction or plume buoyancy during that time, the plume could potentially be over- or under-sampled. Figure 4 demonstrates two or three separated plume maxima on both 20 August (Fig. 4a) and 2 September (Fig. 4b). On both flights the progression of the flight path increased in altitude level upward from near the surface to ~ 1.5 km. Hence

AMTD
8, 4769–4816, 2015

the separation of plume maxima could be due to turbulent fluctuation and large scale eddies, multiple plumes, or a sudden change in plume position, which would result in oversampling of the same plume. In the case of the 20 August flight, this drift would need to be approximately 1 km to the south (decreasing *s* on the east wall in Fig. 4a) and 400 m upward in the duration of one level track completion. In the case of the 2 September flight, the plume would need to move 300 m upward within 11 to 12 min.

Figure 7 shows the wind speeds, wind direction, and temperatures measured at the two towers (http://www.wbea.org) located between the facility and Fort McMurray. During the 20 August flight (Fig. 7a), wind speeds and direction appear consistent at these locations. Temperature rises consistently throughout the two hour duration by approximately 3 °C. Based on these measurements, it is unlikely that a major shift would occur in plume position, as there is no apparent shift to a more northerly flow and an increase in air temperature would cause a relative decrease in plume buoyancy, resulting in undersampling instead of oversampling as the aircraft altitude increases.

During the 2 September flight (Fig. 7b) a shift in winds and temperature is apparent resulting in higher wind speeds, a 3.5 °C drop in air temperature, and a shift from WNW to N winds. A decrease in air temperature could result in a sudden increase in plume buoyancy, which would move the plume upward during the box flight. A shift from westerly to northerly wind speeds would result in a shift in the plume position to the west (decreasing *s* on the south wall in Fig. 4b), so that the higher plume (presumably sampled later) would be west relative to the lower plume (presumable sampled before). This shift in lateral plume position is not seen in Fig. 4b, suggesting that the small shift in wind speed and direction has no apparent effect on the measurements.

4.3 Comparison to industry-reported SO_2 emissions

Individual stack emission rates of SO_2 on a minute-by-minute basis were provided by CNRL for the two flight dates. Using average wind speed and direction and approximate distance from the stack to the box-wall, we estimate a delay of approximately 30 min

AMTD
8, 4769–4816, 2015

between plume emission and interception by the aircraft on 20 August, and 20 min between emission and interception by the aircraft on 2 September.

During the aircraft box flight time period of 10:31 to 12:41 LT on 20 August and adjusting for the 30 min. between plume emission and interception by the aircraft, the minute-by-minute SO_2 emissions give an average emission rate of 12.20 $t\,h^{-1}$. Our TERRA derived SO_2 emission rate is 12.79 $t\,h^{-1}$, with an estimated uncertainty of 2 %. This difference of 4.8 % is higher than the estimated 2 % uncertainty associated with the emission calculation on this day; however, it is possible that the difference of 4.8 % is real and due to non-stack sources of SO_2, such as gas combustion or oxidation of the sulphur stockpile in the facility.

For 2 September, the minute-by-minute SO_2 emission rates from CNRL give an average of 0.224 $t\,h^{-1}$ during the aircraft box flight duration of 11:18 to 14:43 LT and accounting for a plume travel time of 20 min. between emission and interception by the aircraft. This is compared to our TERRA derived SO_2 emission rate of 0.249 $t\,h^{-1}$, with an uncertainty of 21 %. The aircraft derived SO_2 emission rate is 11 % higher (within the estimated uncertainty) but the absolute difference is small at 0.025 $t\,h^{-1}$. This difference may be either due to non-stack SO_2 emissions at the CNRL facility, or due to the uncertainties in the aircraft derived emission rates.

5 Conclusions

The results presented above demonstrate the relative importance of terms in the mass balance equation and potential sources of uncertainty in the emission rate calculations. For a low-background compound, such as SO_2, the horizontal advection is by far the most significant term. In contrast, CH_4 has large background levels and a small incremental concentration due to facility emissions. For CH_4, the significance of the vertical advection and mass density change terms ($E_{C,V}$ and $E_{C,M}$) highlight the potential disadvantages in using simplified techniques to estimate emission rate, such as single height transects or single screens. For example, in the case of a surface-based emit-

AMTD
8, 4769–4816, 2015

ted compound such as CH_4, failure to include advective fluxes through the box top (with proper background subtraction) can result in apparent negative emission rates.

The comparison of interpolation techniques demonstrates that kriging is superior to IDW or natural neighbour interpolations. Although our example simulations demonstrate that kriging can overestimate the average real values slightly (~ 1 %), the uncertainty is small compared to other unknowns.

The conditions of 20 August are clearly reproduced by the TERRA SO_2 emissions calculation. For this day the SO_2 emissions show weak dependence (< 1 % difference) on the method of extrapolation to the surface. The emissions calculated over this 2 h and 10 min period are 4.8 % higher than minute-by-minute emissions (12.20 $t\,h^{-1}$) reported by CNRL. This difference could be due to non-stack sources of SO_2 not included in the CNRL reported values. During normal SO_2 capture operations on 2 September, the CNRL reported value (0.224 $t\,h^{-1}$) is within the range of TERRA calculated emissions (0.22 to 0.27 $t\,h^{-1}$), and is within 11 % of the average TERRA calculated value (0.248 $t\,h^{-1}$).

The TERRA calculated CH_4 emissions show a stronger dependence on the choice of near-surface interpolation methods, as would be expected for a compound emitted from the surface. Although there is some uncertainty near the surface, validation of this emission calculation is demonstrated by the similar values in CH_4 emission rate estimates for the two days. Values based on varying inputs within a range of uncertainty give emission rates between 3.08 to 4.23 $t\,h^{-1}$ on 20 August and from 3.23 to 3.99 $t\,h^{-1}$ on 2 September. Based on these values the CH_4 emission rate is estimated to be $3.7 \pm 0.6\,t\,h^{-1}$, with no significant variation between the dates measured.

The results of this study demonstrate that uncertainty in the emission rate calculation is very low (~ 2 %) for plumes which are entirely captured within the sampling region. For plumes with high near-surface concentrations uncertainties are estimated at approximately 20 %. These uncertainties could be improved significantly with simultaneous ground level measurements, especially directly downwind of the emissions source.

AMTD
8, 4769–4816, 2015

Appendix

Equations (5) and (7) are derived by differentiating $\rho_{air} = p/RT$ with respect to time to give

$$\frac{d\rho_{air}}{dt} = \frac{dp}{dt}\frac{1}{RT} - \frac{dT}{dt}\frac{p}{RT^2} = \rho_{air}\left(\frac{dp}{dt}\frac{1}{p} - \frac{dT}{dt}\frac{1}{T}\right) \approx \frac{\rho_{air}}{\Delta t}\left(\frac{\Delta p}{p} - \frac{\Delta T}{T}\right)$$

where ΔT and Δp are the change in temperature and pressure over time duration Δt, and p and T are the average pressure and temperature for the time duration.

The following is a demonstration of the weak dependence of the estimated emissions rate on temperature and pressure changes. The advective flux through the box top is determined by solving Eq. (1) for $E_{air,V}$ and substituting into the $E_{C,V}$ term as

$$E_{C,V} = M_R \chi_{C,Top}\left(E_{air,M} - E_{air,H}\right).$$

Equation (1) can then be rewritten as

$$E_C = E_{C,H} + E_{C,HT} + \left[M_R \chi_{C,Top}\left(E_{air,M} - E_{air,H}\right)\right] + E_{C,VT} + E_{C,VD} - E_{C,M}.$$

Substituting the volume integrals (Table 2) for $E_{air,M}$ and $E_{C,M}$ and collecting terms gives

$$E_C = E_{C,H} + E_{C,HT} + M_R \chi_{C,Top} E_{air,H} + E_{C,VT} + E_{C,VD} - M_R \iiint_{Volume} \left(\chi_C - \chi_{C,Top}\right)\frac{d\rho_{air}}{dt} dx dy dz.$$

Hence the effect of the pressure and temperature change on the emission rate is proportional to the difference between the mixing ratio within the box (χ_C) and the box-top mixing ratio ($\chi_{C,Top}$). This result implies that any change in density within the box will modify the estimated emission rate proportionally to the excess mixing ratio, above the "background" level. Hence changes in $d\rho_{air}/dt$ of more than ±50 % result in small changes in the estimated emission rate, ranging from −2 and 5 % as shown in Tables 7 and 8.

AMTD
8, 4769–4816, 2015

Acknowledgements. The authors wish to thank the NRC-FRL flight crew of the Convair 580 for making the airborne study possible, in particular the pilots for carrying out the flight patterns that made the development of this algorithm possible. Stewart Cober directed the 20 August flight; Jeff Brook, Matthew Bastian, Anne Marie Macdonald, Paul Makar, Craig Stroud, John Liggio, Peter Liu, Amy Leithead, Samar Moussa, Richard Mittermeier, and Rob McLaren contributed to the success of the airborne measurement program. Funding for the airborne study over the oil sands region was provided in part by Environment Canada's Clean Air Regulatory Agenda (CARA). The authors thank Wood Buffalo Environmental Association (WBEA) for use of the meteorological tower data (open access on the web site), the community of Fort McKay for the support of the Oskiôtin ground site at Fort McKay, and CNRL for the provision of SO_2 emissions data and stack height information.

References

Alfieri, S., Amato, U., Carfora, M. F., Esposito, M., and Magliulo, V.: Quantifying trace gas emissions from composite landscapes: a mass-budget approach with aircraft measurements, Atmospheric Environment, 44, 1866–1876, 2010.

Cambaliza, M. O. L., Shepson, P. B., Caulton, D. R., Stirm, B., Samarov, D., Gurney, K. R., Turnbull, J., Davis, K. J., Possolo, A., Karion, A., Sweeney, C., Moser, B., Hendricks, A., Lauvaux, T., Mays, K., Whetstone, J., Huang, J., Razlivanov, I., Miles, N. L., and Richardson, S. J.: Assessment of uncertainties of an aircraft-based mass balance approach for quantifying urban greenhouse gas emissions, Atmos. Chem. Phys., 14, 9029–9050, doi:10.5194/acp-14-9029-2014, 2014.

Canadian Natural Resources Ltd: Canadian Natural 2012 Stewardship Report to Stakeholders, available at: http://www.cnrl.com/upload/media_element/692/02/2012-stewardship-report_web.pdf (last access: 4 May 2014), 2014.

cnrl.com: available at: http://www.cnrl.com/operations/north-america/horizon-oil-sands.html (last access: 4 May 2014), 2014.

Erisman, J. W. and Baldocchi, D.: Modelling dry deposition of SO_2, Tellus B, 46, 159–171, 1994.

AMTD
8, 4769–4816, 2015

Flesch, T. K., Wilson, J. D., Harper, L. A., Crenna, B. P., and Sharpe, R. R.: Deducing ground-air emissions from observed trace gas concentrations: a field trial, J. Appl. Meteorol., 43, 487–502, 2004.

Garratt, J. R.: The Atmospheric Boundary Layer, Cambridge University Press, Cambridge, 1994.

Isaaks, E. H. and Srivastava, R. M.: An Introduction to Applied Geostatistics, Oxford University Press, Oxford, 1989.

Kalthoff, N., Corsmeier, U., Schmidt, K., Kottmeier, C., Fiedler, F., Habram, M., and Slemr, F.: Emissions of the city of Augsburg determined using the mass balance method, Atmos. Environ., 36, 19–31, 2002.

Karion, A., Sweeney, C., Pétron, G., Frost, G., Hardesty, R. M., Kofler, J., Miller, B. R., Newberger, T., Wolter, S., Banta, R., Brewer, A., Dlugokencky, E., Lang, P., Montzka, S. A., Schnell, R., Tans, P., Trainer, M., Zamora, R., and Conley, S.: Methane emissions estimate from airborne measurements over a western United States natural gas field, Geophys. Res. Lett., 40, 4393–4397, doi:10.1002/grl.50811, 2013.

Mays, K. L., Shepson, P. B., Stirm, B. H., Karion, A., Sweeney, C., and Gurney, K. R.: Aircraft-based measurements of the carbon footprint of Indianapolis, Environ. Sci. Technol., 43, 7816–7823, 2009.

Panitz, H.-J., Nester, K., and Fiedler, F.: Mass budget simulation of NO_x and CO for the evaluation of calculated emissions for the city of Augsburg (Germany), Atmos. Environ., 36, 33–51, 2002.

Peischl, J., Ryerson, T. B., Brioude, J., Aikin, K. C., Andrews, A. E., Atlas, E., Blake, D., Daube, B. C., de Gouw, J. A., Dlugokencky, E., Frost, G. J., Gentner, D. R., Gilman, J. B., Goldstein, A. H., Harley, R. A., Holloway, J. S., Kofler, J., Kuster, W. C., Lang, P. M., Novelli, P. C., Santoni, G. W., Trainer, M., Wofsy, S. C., and Parrish, D. D.: Quantifying sources of methane using light alkanes in the Los Angeles Basin, California, J. Geophys. Res., 118, 4974–4990, doi:10.1002/jgrd.50413, 2013.

Ryerson, T. B., Trainer, M., Holloway, J. S., Parrish, D. D., Huey, L. G., Sueper, D. T., Frost, G. J., Donnelly, S. G., Schauffler, S., Atlas, E. L., Kuster, W. C., Goldan, P. D., Hübler, G., Meagher, J. F., and Fehsenfeld, F. C.: Observations of ozone formation in power plant plumes and implications for ozone control strategies, Science, 27, 719–723, doi:10.1126/science.1058113, 2001.

AMTD
8, 4769–4816, 2015

Sibson, R.: A brief description of natural neighbor interpolation, Chapt. 2, in: Interpreting Multivariate Data, edited by: Barnett, V., John Wiley, Chichester, 21–36, 1981.
Trainer, M., Ridley, B. A., Buhr, M. P., Kok, G., Walega, J., Hübler, G., Parrish, D. D., and Fehsenfeld F. C.: Regional ozone and urban plumes in the southeastern United States: Birmingham, a case study, J. Geophys. Res., 100, 18823–18834, doi:10.1029/95JD01641, 1995.
Turnbull, J. C., Karion, A., Fischer, M. L., Faloona, I., Guilderson, T., Lehman, S. J., Miller, B. R., Miller, J. B., Montzka, S., Sherwood, T., Saripalli, S., Sweeney, C., and Tans, P. P.: Assessment of fossil fuel carbon dioxide and other anthropogenic trace gas emissions from airborne measurements over Sacramento, California in spring 2009, Atmos. Chem. Phys., 11, 705–721, doi:10.5194/acp-11-705-2011, 2011.
Vinuesa, J.-F. and Galmarini, S.: Turbulent dispersion of non-uniformly emitted passive tracers in the convective boundary layer, Bound.-Lay. Meteorol., 133, 1–16, 2009.
Walter, D., Heue, K.-P., Rauthe-Schöch, A., Brenninkmeijer, C. A. M., Lamsal, L. N., Krotkov, N. A., and Platt, U.: Flux calculation using CARIBIC DOAS aircraft measurements: SO_2 emission of Norilsk, J. Geophys. Res., 117, D11305, doi:10.1029/2011JD017335, 2012.
Wratt, D. S., Gimson, N. R., Brailsford, G. W., Lassey, K. R., Bromley, A. M., and Bell, M. J.: Estimating regional methane emissions from agriculture using aircraft measurements of concentration profiles, Atmos. Environ., 35, 497–508, 2001.
Zhang, L., Brook, J. R., and Vet, R.: A revised parameterization for gaseous dry deposition in air-quality models, Atmos. Chem. Phys., 3, 2067–2082, doi:10.5194/acp-3-2067-2003, 2003.

AMTD
8, 4769–4816, 2015

Table 1. Reported studies of ground source emission estimations from aircraft-based measurements.

Reference	Measurement Technique	Measured Compound(s)
Turnbull et al. (2009)	Single Height Transect	CO_2, CH_4, CO
Peischl et al. (2013)	Single Height Transect	CO_2, CH_4, CO
Karion et al. (2013)	Single Height Transect	CH_4
Wratt et al. (2001)	Up and downwind spirals	CH_4
Mays et al. (2009)	Single Screen	CO_2, CH_4
Cambaliza et al. (2013)	Single Screen	CO_2, CH_4
Walter et al. (2012)	Single Screen (DOAS)	SO_2
Kalthoff et al. (2002)	Box	CO, NO_x
Alfieri et al. (2010)	Box	CO_2

AMTD
8, 4769–4816, 2015

Table 2. Terms from Eqs. (1) and (2) used to solve for the total emission rate, E_C. The necessary input variables are listed with their functional dependence. See text for explanation of variables.

Term	Integral	Description	Input variables
$E_{\mathrm{air,H}}$	$\iint_{\mathrm{Sides}} \rho_{\mathrm{air}} U_{\perp} \mathrm{d}s\mathrm{d}z$	Integrated horizontal advection of air mass	$U_{\mathrm{N}}(s,z)$, $U_{\mathrm{E}}(s,z)$, $\rho_{\mathrm{air}}(s,z)$, $s(x,y)$
$E_{\mathrm{air,M}}$	$\iiint_{\mathrm{Volume}} \frac{\mathrm{d}\rho_{\mathrm{air}}}{\mathrm{d}t} \mathrm{d}x\mathrm{d}y\mathrm{d}z$	Change in air mass within volume	$T(t)$, $p(t)$, $\rho_{\mathrm{air}}(z)$
$E_{\mathrm{air,V}}$	$\iint_{\mathrm{Top}} \rho_{\mathrm{air}} w \mathrm{d}x\mathrm{d}y$	Integrated advection of air mass through the box top	$E_{\mathrm{air,H}}$, $E_{\mathrm{air,L}}$
$E_{C,\mathrm{V}}$	$M_{\mathrm{R}} \chi_{C,\mathrm{Top}} \iint_{\mathrm{Top}} \rho_{\mathrm{air}} w \mathrm{d}x\mathrm{d}z$	Integrated advection of SO_2 or CH_4 mass through the box top	$\chi_{C,\mathrm{Top}}$,$E_{\mathrm{air},T}$
$E_{C,\mathrm{H}}$	$M_{\mathrm{R}} \iint_{\mathrm{Sides}} \chi_C \rho_{\mathrm{air}} U_{\perp} \mathrm{d}s\mathrm{d}z$	Integrated horizontal advection of SO_2 or CH_4 mass	$U_{\mathrm{N}}(s,z)$, $U_{\mathrm{E}}(s,z)$, $\rho_{\mathrm{air}}(s,z)$, $s(x,y)$ $\chi_{\mathrm{SO_2}}(s,z)$ or $\chi_{\mathrm{CH_4}}(s,z)$
$E_{C,\mathrm{HT}}$	$-M_{\mathrm{R}} \iint_{\mathrm{Sides}} K_x \frac{\mathrm{d}\chi_C}{\mathrm{d}x_{\perp}} \rho_{\mathrm{air}} \mathrm{d}s\mathrm{d}z$	Integrated horizontal turbulent flux of SO_2 or CH_4 mass	Estimated value with $\chi_{\mathrm{SO_2}}(s,z)$ or $\chi_{\mathrm{CH_4}}(s,z)$
$E_{C,\mathrm{VT}}$	$M_{\mathrm{R}} \iint_{\mathrm{Top}} \Delta\chi \rho_{\mathrm{air}} w_e \mathrm{d}x\mathrm{d}y$	Integrated turbulent flux of SO_2 or CH_4 mass through the box top	Estimated value with $\chi_{\mathrm{SO_2}}(s,z_{\mathrm{Top}})$ or $\chi_{\mathrm{CH_4}}(s,z_{\mathrm{Top}})$
$E_{C,\mathrm{VD}}$	$M_{\mathrm{R}} \iint_{\mathrm{Bottom}} \chi_{\mathrm{sur}} \rho_{\mathrm{air}} V_{\mathrm{d}} \mathrm{d}x\mathrm{d}y$	Deposition rate of SO_2 or CH_4 mass to the surface	Estimated value with $\chi_{\mathrm{SO_2}}(s,z_g)$ or $\chi_{\mathrm{CH_4}}(s,z_g)$
$E_{C,\mathrm{M}}$	$M_{\mathrm{R}} \iiint_{\mathrm{Volume}} \chi_C \frac{\mathrm{d}\rho_{\mathrm{air}}}{\mathrm{d}t} \mathrm{d}x\mathrm{d}y\mathrm{d}z$	Change in SO_2 or CH_4 mass with time within volume	Estimated value with $T(t)$, $p(t)$, and $\rho_{\mathrm{air}}(z)$
$E_{C,\mathrm{X}}$	$M_{\mathrm{R}} \iiint_{\mathrm{Volume}} \frac{\mathrm{d}\chi_C}{\mathrm{d}t} \rho_{\mathrm{air}} \mathrm{d}x\mathrm{d}y\mathrm{d}z$	Change in SO_2 or CH_4 mixing ratio with time within volume	Estimated with wind speed, chemistry, and source location

AMTD
8, 4769–4816, 2015

Table 3. Parameters used in Eq. (8) for each simulation scenario and plume number (i). The corresponding panel (a, b, or c) in Fig. 3 is also given.

Fig. 3	Interpolation	i	$s_{o,i}$ [m]	$z_{o,i}$ [m]	$\sigma_{s,i}$ [m]	$\sigma_{z,i}$[m]	β
(a)	Single elevated source	1	22 000	950	2000	150	30
(b)	Two elevated sources	1	22 000	900	1200	140	20
		2	19 500	600	800	120	10
(c)	Ground source	1	20 000	300	800	400	0

AMTD
8, 4769–4816, 2015

Table 4. Statistical comparison of interpolation techniques: inverse distance weighting (IDW), nearest-neighbour (NN) and kriging. The 20 August flight positions are used with three simulated emissions scenarios: (1) a single elevated plume; (2) two overlapping elevated plumes; and (3) a plume from a ground source. Different surface extrapolation methods are used based on the plume location (see Sect. 3.1). The statistics are the ratio of interpolated average (μ) to the simulate average (μ_{sim}), the ratio of root-mean squared error (E_{rms}) to the simulated average (μ_{sim}), and the coefficient of correlation (r^2).

Scenario	Extrapolation Method	Statistic	IDW	NN	Kriging
1	Zero	μ/μ_{sim}	0.988	0.996	0.998
		E_{rms}/μ_{sim}	0.259	0.151	0.086
		r^2	0.985	0.996	0.998
2	Zero	μ/μ_{sim}	0.955	0.955	0.954
		E_{rms}/μ_{sim}	0.434	0.400	0.374
		r^2	0.967	0.972	0.976
2	Constant	μ/μ_{sim}	1.077	1.083	1.081
		E_{rms}/μ_{sim}	0.544	0.537	0.529
		r^2	0.950	0.950	0.953
2	Zero-Constant	μ/μ_{sim}	1.013	1.016	1.014
		E_{rms}/μ_{sim}	0.254	0.194	0.134
		r^2	0.989	0.994	0.997
3	Linear-Fit	μ/μ_{sim}	1.043	1.065	1.028
		E_{rms}/μ_{sim}	0.409	0.470	0.317
		r^2	0.994	0.991	0.996
3	Exponential-Fit	μ/μ_{sim}	1.000	1.004	0.999
		E_{rms}/μ_{sim}	0.293	0.259	0.177
		r^2	0.996	0.997	0.998

AMTD
8, 4769–4816, 2015

Table 5. Mass balance terms for air (Eq. 2) in units of 10^9 kg h^{-1}, with $E_{air,H} = E_{air,H,out} - E_{air,H,in}$.

Term	20 Aug	2 Sep
$E_{air,H,in}$	479.6	722.6
$E_{air,H,out}$	394.6	657.9
$E_{air,M}$	−1.4	1.3
$E_{air,V}$	83.6	66.0

AMTD
8, 4769–4816, 2015

Table 6. Mass balance terms for SO_2 and CH_4 (Eq. 1), with $E_{C,H} = E_{C,H,out} - E_{C,H,in}$.

Term	SO_2 [$t\,h^{-1}$]		CH_4 [$t\,h^{-1}$]	
	20 Aug	2 Sep	20 Aug	2 Sep
$E_{C,H,in}$	0.226	0.148	501.1	766.2
$E_{C,H,out}$	12.890	0.395	416.5	701.3
$E_{C,V}$	0.003	< 0.001	87.3	69.9
$E_{C,HT}$	0.004	< 0.001	0.00	0.00
$E_{C,VT}$	0	0	0.07	0.24
$E_{C,VD}$	0	0	0.00	0.00
$E_{C,M}$	−0.015	< 0.001	−1.49	1.53
$E_{C,X}$	−0.097	−0.002	0	0
E_C	12.79	0.249	4.21	3.79

AMTD
8, 4769–4816, 2015

Table 7. SO_2 emission rate (E_C) in $t\,h^{-1}$ calculated for varying inputs. The base case is a zero-to-constant surface extrapolation, with average temperature and pressure ratio. Percent change relative to the base case is also listed.

Scenario	20 Aug	% Change	2 Sep	% Change
Base Case (zero-to-constant)	12.79		0.249	
Constant extrapolation to surface	12.83	0.4 %	0.273	9.9 %
Zero extrapolation to surface	12.75	−0.3 %	0.219	−11.8 %
Lowest T, P ratio	12.78	0.0 %	0.249	−0.1 %
Highest T, P ratio	12.79	0.0 %	0.249	0.3 %
Constant near-surface wind	12.79	0.0 %	0.251	1.0 %
Increased $\chi_{C,\mathrm{Top}}$	12.79	0.0 %	0.251	1.0 %
Decreased $\chi_{C,\mathrm{Top}}$	12.78	0.0 %	0.246	−1.0 %

AMTD
8, 4769–4816, 2015

Table 8. CH_4 emission rate (E_C) in $t\,h^{-1}$ calculated for varying inputs. The base case is an exponential surface extrapolation, with average temperature and pressure ratio.

Scenario	20 Aug	% Change	2 Sep	% Change
Base Case (exponential-fit)	4.21		3.79	
Constant extrapolation to surface	3.08	−26.8 %	3.75	−1.1 %
Linear-fit extrapolation to surface	3.01	−28.5 %	3.43	−18.6 %
Exponential in/Constant out	3.08	−26.8 %	3.23	−15.0 %
Lowest T, P ratio	4.21	−0.1 %	3.72	−1.9 %
Highest T, P ratio	4.21	0.0 %	3.99	5.1 %
Constant near-surface wind	4.23	0.5 %	3.81	0.5 %
Increased $\chi_{C,\mathrm{Top}}$	4.23	0.4 %	3.82	0.8 %
Decreased $\chi_{C,\mathrm{Top}}$	4.19	−0.4 %	3.76	−0.8 %

AMTD
8, 4769–4816, 2015

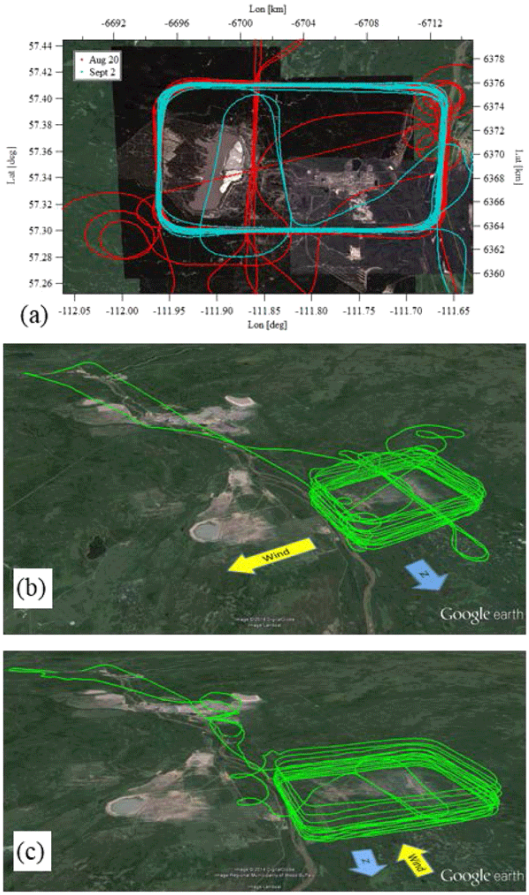

Figure 1. A composite Google image **(a)** shows the path of the 20 August (red) and 2 September (cyan) flights. Google Earth images demonstrate the path of **(b)** the 20 August flight and **(c)** the 2 September flight. The yellow arrow shows wind direction, the blue arrow shows north. Map image data provided by CNES/SPOT, Digital Globe, and Google.

AMTD
8, 4769–4816, 2015

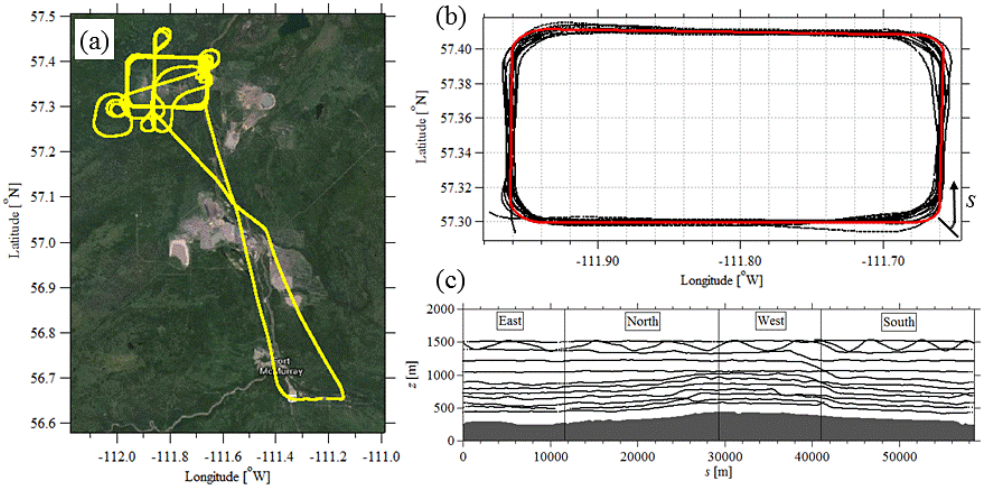

Figure 2. The mapping of aircraft position during the box flight to the box walls for the 20 August flight showing **(a)** the complete flight path, **(b)** the box flight aircraft position data (black dots) and least squares fit (red line), and **(c)** the unwrapped screen in the horizontal path length (s) and height (z) dimensions. The ground elevation ($z_g(s)$) beneath the flight path fit is shown in grey shading **(c)**.

AMTD
8, 4769–4816, 2015

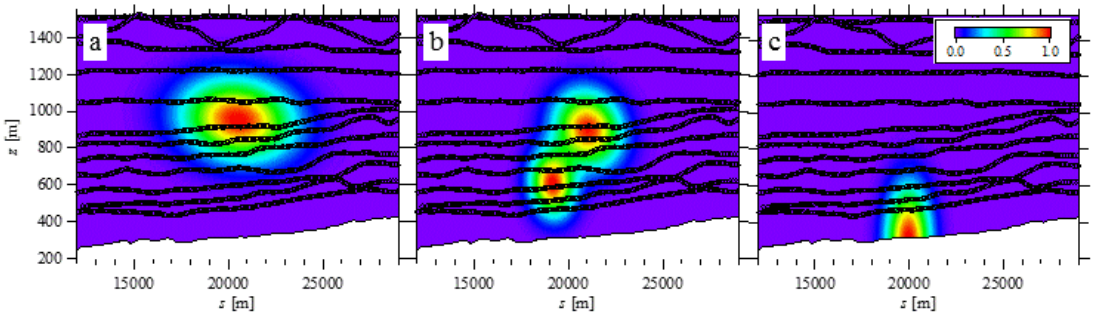

Figure 3. The simulated emissions scenarios of Table 3 and Eq. (10) with the flight positions of the 20 August flight (open circles) for **(a)** an elevated source, **(b)** two elevated sources, and **(c)** a ground source. The values at the flight positions are then used with IDW, natural neighbour, and kriging interpolation to attempt to recreate the original plume image.

AMTD
8, 4769–4816, 2015

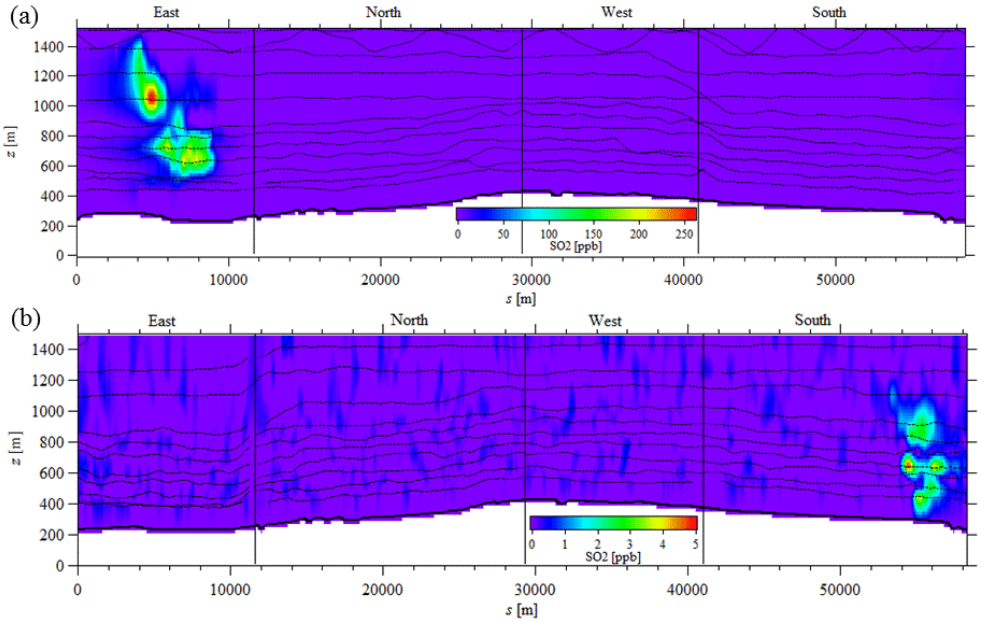

Figure 4. Interpolated SO_2 mixing ratios for the 20 August **(a)** and 2 September **(b)** flights. Note that the colour scales are different. The flight path is superimposed (black dots). The near-surface values are estimated using a zero-constant extrapolation which varies linearly from the lowest measurement to a zero value at the surface.

AMTD
8, 4769–4816, 2015

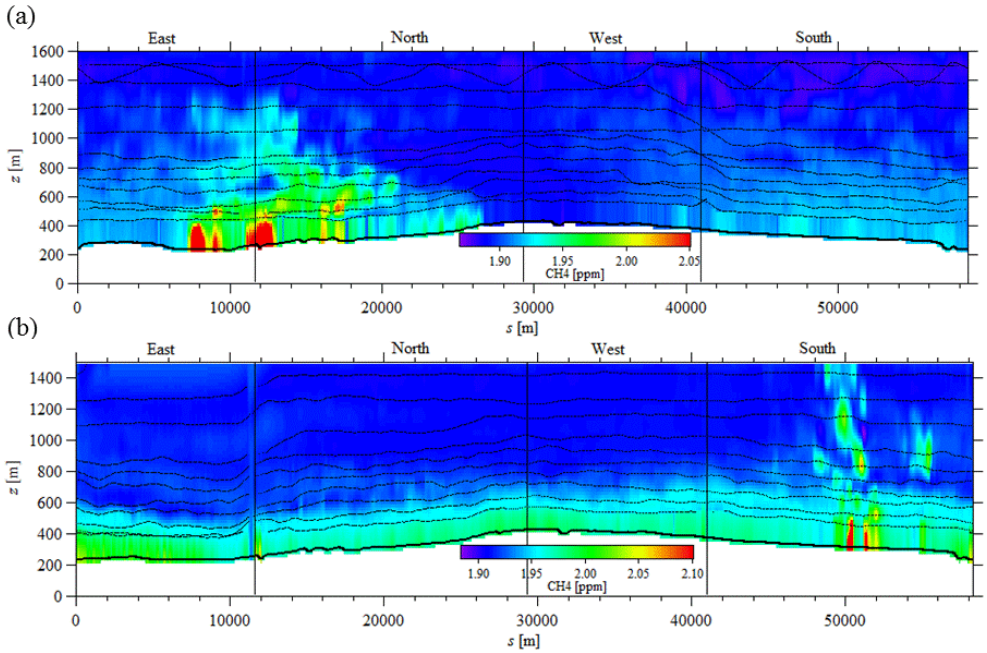

Figure 5. Interpolated CH_4 mixing ratios for the 20 August **(a)** and 2 September **(b)** flights. The flight path is superimposed (black dots). Values below the lowest flight path are extrapolated with an exponential fit (Eq. 9).

AMTD
8, 4769–4816, 2015

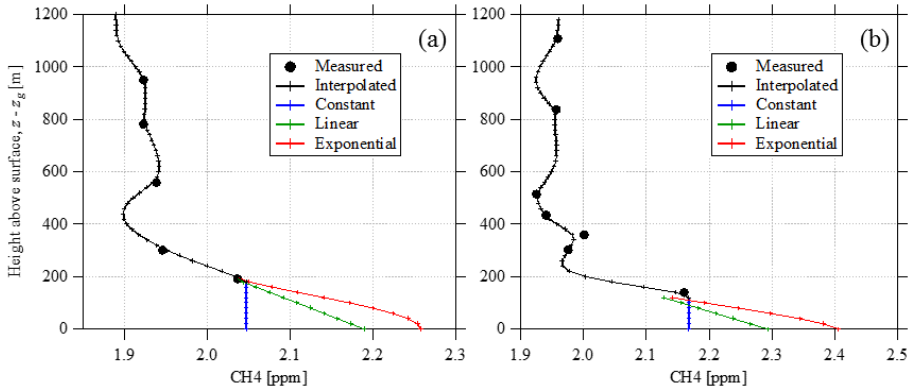

Figure 6. CH_4 mixing ratios with height above ground for the 20 August flight **(a)** at $s = 12.4$ km and for the 2 September flight **(b)** at $s = 50.4$ km. Measured values within ±40 m (Δs) are shown as dots, interpolated values ($z > z_L(s)$, black lines) are compared to extrapolated values ($z < z_L(s)$) for constant (blue), linear-fit (green), and exponential-fit (red) values. Background values on each day were approximately 1.9 ppm.

AMTD
8, 4769–4816, 2015

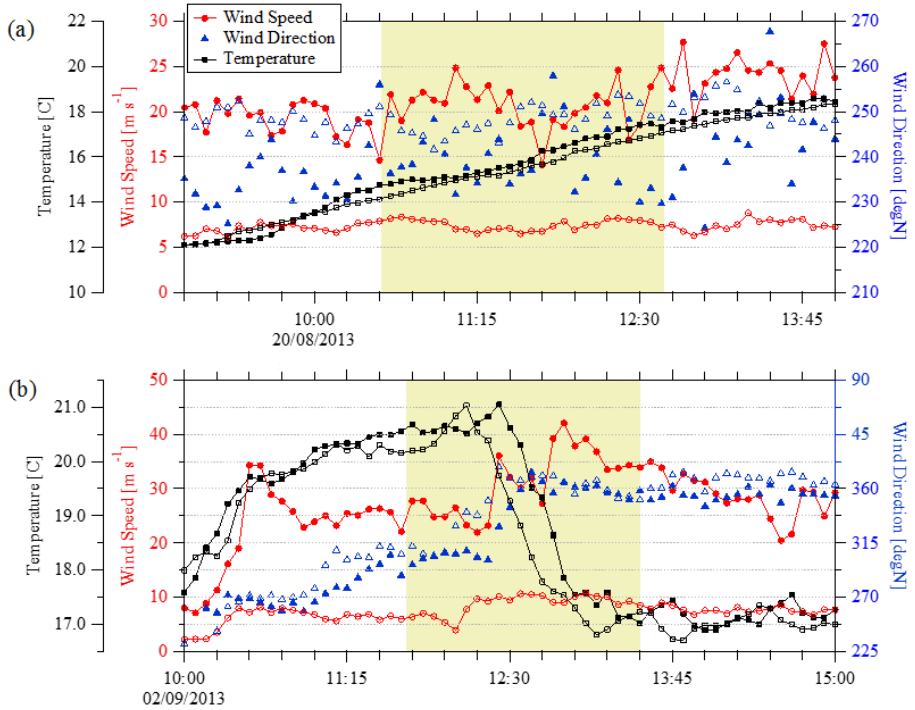

Figure 7. Wind speed (circles), direction (triangles), and temperature (squares) as recorded by two WBEA towers. Open symbols are at AMS03 (57.032° N, 111.505° W) at a height of 167 m a.g.l. and closed symbols are at AMS05 (56.969° N, 111.482° W) at a height of 75 m a.g.l. The shaded area shows the duration of the flight box on 20 August **(a)** and 2 September **(b)**. Times are LT (MDT).

AMTD
8, 4769–4816, 2015